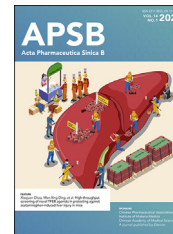




Chinese Pharmaceutical Association
Institute of Materia Medica, Chinese Academy of Medical Sciences

Acta Pharmaceutica Sinica B

www.elsevier.com/locate/apsb
www.sciencedirect.com



ORIGINAL ARTICLE

Structure-based development of potent and selective type-II kinase inhibitors of RIPK1



Ying Qin^{a,b,†}, Dekang Li^{a,b,†}, Chunting Qi^{a,†}, Huaijiang Xiang^{a,b},
Huyan Meng^{a,b}, Jingli Liu^a, Shaoqing Zhou^{a,b}, Xinyu Gong^{b,c},
Ying Li^{b,c}, Guifang Xu^a, Rui Zu^a, Hang Xie^d, Yechun Xu^{b,e}, Gang Xu^f,
Zheng Zhang^f, Shi Chen^g, Lifeng Pan^c, Ying Li^{a,*}, Li Tan^{a,c,*}

^aInterdisciplinary Research Center on Biology and Chemistry, Shanghai Institute of Organic Chemistry, Chinese Academy of Sciences, Shanghai 201210, China

^bUniversity of Chinese Academy of Sciences, Beijing 100049, China

^cState Key Laboratory of Chemical Biology, Shanghai Institute of Organic Chemistry, Chinese Academy of Sciences, Shanghai 200032, China

^dSchool of Chinese Materia Medica, Nanjing University of Chinese Medicine, Nanjing 210023, China

^eState Key Laboratory of Drug Research, Shanghai Institute of Materia Medica, Chinese Academy of Sciences, Shanghai 201203, China

^fInstitute of Hepatology, National Clinical Research Center for Infectious Disease, Shenzhen Third People's Hospital, the Second Affiliated Hospital, School of Medicine, Southern University of Science and Technology, Shenzhen 518112, China

^gDepartment of Burn and Plastic Surgery, Shenzhen Institute of Translational Medicine, Shenzhen University Medical School, Shenzhen Second People's Hospital, the First Affiliated Hospital of Shenzhen University, Shenzhen 518035, China

Received 21 May 2023; received in revised form 21 October 2023; accepted 26 October 2023

KEY WORDS

RIPK1;
Necroptosis;
Type-II kinase inhibitors;
Rational design;
Lead optimization;

Abstract Receptor-interacting serine/threonine-protein kinase 1 (RIPK1) functions as a key regulator in inflammation and cell death and is involved in mediating a variety of inflammatory or degenerative diseases. A number of allosteric RIPK1 inhibitors (RIPK1i) have been developed, and some of them have already advanced into clinical evaluation. Recently, selective RIPK1i that interact with both the allosteric pocket and the ATP-binding site of RIPK1 have started to emerge. Here, we report the rational development of a new series of type-II RIPK1i based on the rediscovery of a reported but mechanistically

*Corresponding authors.

E-mail addresses: liyingsioc@sioc.ac.cn (Ying Li), tanli@sioc.ac.cn (Li Tan).

†These authors made equal contributions to this work.

Peer review under the responsibility of Chinese Pharmaceutical Association and Institute of Materia Medica, Chinese Academy of Medical Sciences.

<https://doi.org/10.1016/j.apsb.2023.10.021>

2211-3835 © 2024 The Authors. Published by Elsevier B.V. on behalf of Chinese Pharmaceutical Association and Institute of Materia Medica, Chinese Academy of Medical Sciences. This is an open access article under the CC BY-NC-ND license (<http://creativecommons.org/licenses/by-nc-nd/4.0/>).

Structure–activity relationship;
Anti-inflammation;
Preclinical drug discovery

atypical RIPK3i. We also describe the structure-guided lead optimization of a potent, selective, and orally bioavailable RIPK1i, **62**, which exhibits extraordinary efficacies in mouse models of acute or chronic inflammatory diseases. Collectively, **62** provides a useful tool for evaluating RIPK1 in animal disease models and a promising lead for further drug development.

© 2024 The Authors. Published by Elsevier B.V. on behalf of Chinese Pharmaceutical Association and Institute of Materia Medica, Chinese Academy of Medical Sciences. This is an open access article under the CC BY-NC-ND license (<http://creativecommons.org/licenses/by-nc-nd/4.0/>).

1. Introduction

Receptor-interacting serine/threonine-protein kinase 1 (RIPK1) plays a key role in inflammatory response and programmed cell death. It is well known as a master regulator in the TNFR1-mediated activations of the pro-survival NF- κ B, the pro-apoptotic FADD-caspase-8, and the pro-necroptotic RIPK3-MLKL signal pathways¹. The kinase activity of RIPK1 has been demonstrated to mediate or aggravate the pathological conditions in a broad set of inflammatory or degenerative diseases, such as sepsis, ischemia, rheumatoid arthritis (RA), inflammatory bowel disease (IBD), psoriasis, multiple sclerosis, amyotrophic lateral sclerosis, and severe COVID-19^{2,3}. Thus, RIPK1 is considered a therapeutic target with great potential, and plenty of RIPK1 inhibitors (RIPK1i) have been developed in the past decade^{2,4,5}.

Facilitated by the robust necroptotic phenotypes induced by TNF α , a large part of RIPK1i was developed based on cell-based high-throughput screening (HTS). Examples of them include Nec-1s (**1**)^{6,7}, the first RIPK1i widely used to interrogate RIPK1 in diverse disease models, GSK2982772 (**2**)⁸, the first RIPK1i to enter clinical trials, RIPA-56 (**3**), GSK'547, and Nec-34 (Fig. 1)^{9–11}. To obtain more optimized RIPK1i, various analogs of **2** had been generated, such as the Takeda compound 22 (**4**), GNE684, R552, and ZB-R-55^{2,4,12–15}. Structural studies discovered that most selective RIPK1i bind to an allosteric and hydrophobic pocket adjacent to the ATP-binding pocket of RIPK1, rendering RIPK1 in an uncommon DLG-out/Glu-out inactive conformation^{16,17}. Additional interactions with the ATP-binding pocket could significantly improve the potency of **2**, especially against mouse RIPK1 (mRIPK1)^{14,15}. These findings

indicated that RIPK1i could be developed as *bona fide* type-II kinase inhibitors (KI) with further improved potency and retained selectivity by concomitantly occupying both binding pockets of the targeted kinases, which could provide novel pharmacophores and potentially advantageous candidates for current clinical drug discovery¹⁸. Early-stage type-II RIPK1i had already been discovered based on HTS (**5**) or structure-guided hybridization (**6**), despite notable flaws^{17,19,20}. Recently, more optimized RIPK1i, such as Zharp1-211 (**7**) and RI-962, had been successfully developed^{21–23}, further supporting the potentials of type-II RIPK1i.

Herein, we report the discovery of a series of potent and selective type-II RIPK1i based on a known RIPK3i and structure-guided rational design. RIPK3 is a major downstream effector and close homolog of RIPK1, but it does not possess the structurally unique hydrophobic pocket as RIPK1²⁴. Two selective RIPK3i, GSK'843 (**8**) and GSK'872 (**9**), were reported to induce apoptosis, with **8** confirmed as a type-I KI based on co-crystal structure determination (Fig. 1)²⁵. In our preliminary studies, **9** could be readily docked into the co-crystal structure of **8**, whereas another RIPK3i, GSK'840 (**10**), was incompatible with the binding mode of **8**, and did not induce apoptosis. These findings led us to speculate that **10** could be a type-II KI and encouraged us to optimize **10** using classical strategies to develop type-II KI. However, initial modification efforts on **10** serendipitously resulted in activity against RIPK1 other than improved potency against RIPK3, eventually leading to the development of *bona fide* type-II RIPK1i in this work. We then discuss the structure–activity relationship (SAR) of these inhibitors and describe the lead optimization of **62**, an orally bioavailable and tolerable type-II

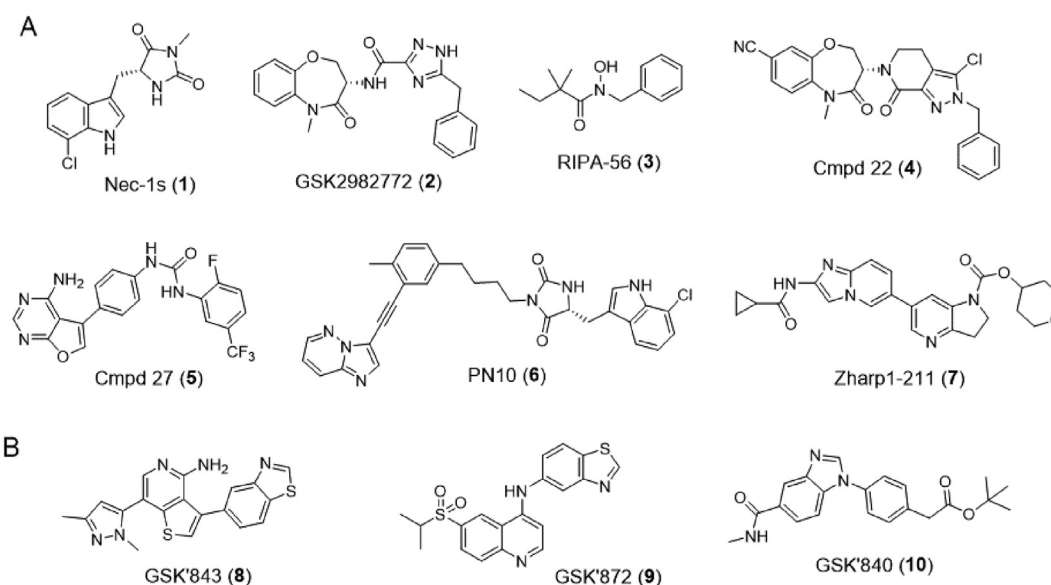


Figure 1 Chemical structures of representative RIPK1i (A) or RIPK3i (B).

RIPK1i, which exhibited extraordinary efficacies in RIPK1-dependent acute and chronic inflammation animal models.

2. Results and discussion

Both RIPK3i **9** and **10** were tested for their protective effects against the cell death of L929 mouse fibroblasts induced by TNF α treatments (Fig. 2A). Consistent with the literature²⁵, treatments with **9** led to aggravated cell death reportedly *via* induction of RIPK3-dependent apoptosis. In contrast, treatments with **10** remarkably protected the L929 cells from cell death caused by TNF α , indicating that **10** might inhibit RIPK3 through a different mechanism compared to **9**. Based on the inconsistent docking results and phenotypic differences in the context of cell death between **9** and **10**, we speculated that **10** might be a type-II KI of RIPK3, with its *tert*-butyl ester moiety interacting with the hydrophobic pocket of RIPK3 near its DFG-motif¹⁸. Then, a *meta*-trifluoromethylaniline-based amide moiety commonly adopted by type-II KI was introduced to replace the *tert*-butyl ester moiety of **10**, yielding a more prototypical type-II inhibitor **11** (Fig. 2B). Replacing the phenylacetamide linkage of **11** with phenylurea or benzamide provided two analogs, **12** and **13**.

Both **11** and **12** showed protective effects similar to **10** in L929 cells, while **13** was relatively weaker (Fig. 2A). These compounds also protected HT-29 human colon cancer cells against necroptosis induced by a cocktail of TNF α , SM164 (cIAP1/2 inhibitor) and zVAD (caspase inhibitor) (Fig. 2C). The Western blot results showed that, in the stimulated HT-29 cells, **11** and **12** at 5 μ mol/L comparably diminished the phosphorylation of RIPK3 and the downstream MLKL as **9** and **10** did, confirming their inhibition of the necroptosis pathway (Fig. 2D). Surprisingly, **11** and **12** also diminished the phosphorylation of the upstream effector RIPK1, whereas **9** or **10** did not at all. On the other hand, **9** and **10** fully protected FKBP-RIPK3-expressing NIH-3T3 cells

from necroptosis caused by AP20187, a compound capable of inducing FKBP dimerization and the consequent RIPK3 activation²⁶, whereas **11** and **12** only exerted partial protection (Fig. 2E). These results indicated that **11** and analogs are RIPK1/3 dual inhibitors.

11 was found to be comparably potent as **1** against mRIPK1 with sub-micromolar EC₅₀ values to protect L929 cells from necroptosis. However, it was almost inactive in the FADD-deficient (FADD^{-/-}) Jurkat human T lymphocyte cells, indicating that it is rather weak against human RIPK1 (hRIPK) (Table 1). To optimize the potency against hRIPK1, an *N*-benzylhydroxylamine group was adopted from a reported RIPK1i, **3**, to replace the general type-II aniline tail, which only slightly improved the potency. Then, the amide bond of **11** was reversed and the triazole moiety of **2** was adopted, which unexpectedly led to a complete loss of potency (**15**). Nevertheless, replacing the 1*H*-1,2,4-triazole ring of **15** with a 1,2,4-oxadiazole ring yielded an inhibitor more selective for hRIPK1, **16**, whereas **17** with a 1,3,4-oxadiazole ring was less potent. **18** with an oxazole ring was better than **17**, while **19** with an isoxazole ring was even better than **16**. Replacing the isoxazole with a *N*-methyl pyrazole (**20**) slightly increased the potency of **19**. On the contrary, **21**, the isomer of **20**, was completely inactive. Notably, increases in the size of the *N*-substituents on the pyrazole were less favored (**22**, **23**). On the other hand, **24** with a 1,2,3-triazole ring showed moderate potency, indicating the naked pyrazole NH of **15** to be disfavored. **25** with a tetrazole ring was even more potent than **24**. However, these analogs of **14** by far, all with a benzyl group located at the *meta*-position on the 5-membered heterocycles, were all weak against mRIPK1. In contrast, **26** with a 5-fluoropyrrole ring and an *ortho*-*N*-benzyl exhibited outstanding potency against both hRIPK1 and mRIPK1. Consistently, the bioisosteric **27** with an *N*-methyl pyrazole and an *ortho*-benzyl showed even better potency.

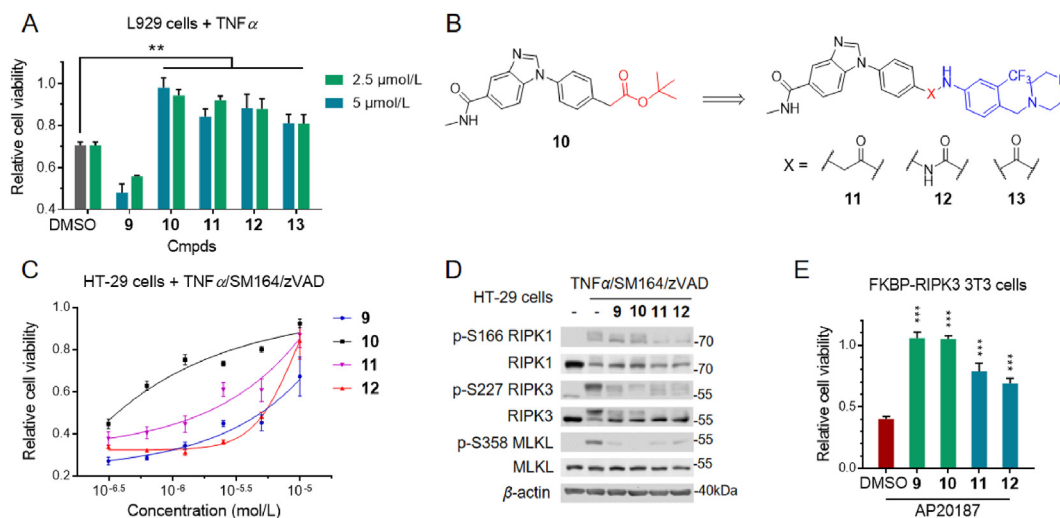
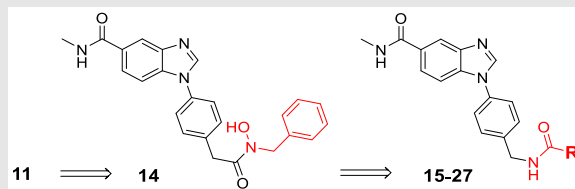


Figure 2 Identification of RIPK1/3 dual inhibitors. (A) Bar graph showing the protective effects of RIPK3i and derivatives in L929 cells. Cells were treated with TNF α at 40 ng/mL in the presence of DMSO or compounds for 15 h before the cell viability test. (B) The chemical structure of the derivatives of **10**. (C) Dose–response curves showing the protective effects of each compound compared to DMSO in HT-29 cells stimulated by TNF α (10 ng/mL), SM164 (25 nmol/L) and zVAD (25 μ mol/L) for 24 h. (D) HT-29 cells stimulated by TNF α , SM164, and zVAD in the presence of DMSO or compounds at 5 μ mol/L for 4 h, then analyzed by Western blotting. (E) Bar graph showing the anti-necroptotic effects of each compound at 10 μ mol/L in FKBP-RIPK3-expressing NIH-3T3 cells. Cells were treated with the FKBP-dimerizing agent, AP20187 (100 nmol/L), in the presence of DMSO or compounds for 15 h before the viability test. All data represent mean \pm SD ($n = 3$); ** $P < 0.01$, *** $P < 0.001$, unpaired Student's *t*-test.

Table 1 Optimization of the tail subunits (R)^a.

Compd.	R	EC ₅₀ (nmol/L) ^b			
		FADD ^{-/-} Jurkat		L929	
		TNFα	T + S	TNFα	T + S
1		94	590	112	689
11		>10,000	>10,000	190	713
14		3805	>10,000	50	98
15		>10,000	>10,000	>10,000	>10,000
16		24	176	962	4735
17		185	1516	>10,000	>10,000
18		70	380	831	3975
19		8.1	113	2138	3348
20		5.1	44	312	2022
21		>10,000	>10,000	>10,000	>10,000
22		5.9	43	n.d.	>10,000
23		109	738	3007	>10,000
24		233	1594	>10,000	>10,000
25		24	150	1106	4310
26		1.7	17	6	34
27		0.5	5.2	20	77

^aData represent means of three replicates.

^bCell viability assays, T = TNFα, S = SM164.

To better understand the pharmacophore of our RIPK1i, we determined the co-crystal structure of the RIPK1–**20** complex at 2.3 Å resolution (PDB 8I2N) (Fig. 3 and Supporting Information Table S1). Unlike **1** and **2** which interact mainly with the hydrophobic pocket adjacent to the DLG-motif of RIPK1 (Fig. 3A), **20** interacts with both the hydrophobic pocket and the ATP-binding pocket (Fig. 3B). Its benzylpyrazole ‘tail’ occupies the allosteric pocket, forcing RIPK1 into a DLG-out/inactive conformation¹⁸. Notably, the α-helix of RIPK1 adopts a ‘Glu-out’ conformation upon binding to **20**, just as it does upon binding to **1** or **2**. In comparison, a previously reported type-II RIPK1i, **5**, binds to RIPK1 in a DLG-out but Glu-in

conformation (Fig. 3C), just as a promiscuous type-II KI, ponatinib, binds to RIPK2²⁷, or a reported type-II RIPK3i binds to RIPK3 (Supporting Information Fig. S1)²⁸. On the other hand, the phenylacetamide linker of **20** helps position its benzimidazole ‘head’ toward the hinge region of RIPK1. Two hydrogen bonds (H-bonds) are formed between **20** and RIPK1: one between the linker carbonyl of **20** and the amide NH of Arg156 in the DLG-motif; another between a nitrogen atom of **20**’s benzimidazole head and the amide NH of Met95 in the hinge (Fig. 3D). Additionally, each subunit of **20** interacts with several surrounding residues through van der Waals forces (Fig. 3E). An intramolecular H-bond may also form a pseudo-

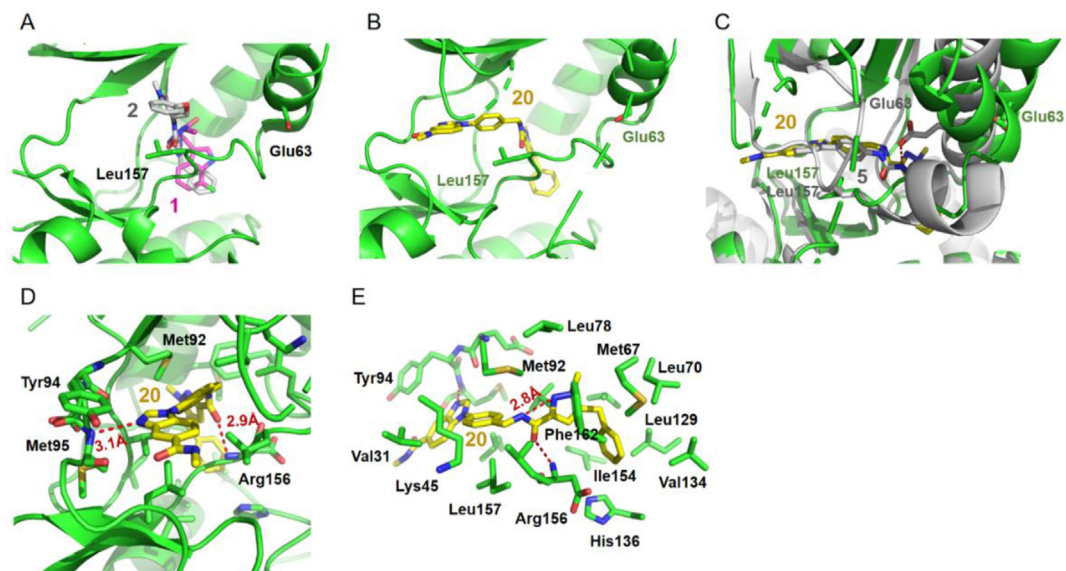


Figure 3 Determination of the co-crystal structure of RIPK1–20 complex. (A) Superimposition of the co-crystal structures of RIPK1 (green ribbons) in complex with **1** (purple sticks, PDB 4ITH) or **2** (grey sticks, PDB 5TX5). (B) The co-crystal structure of RIPK1 (green ribbons) in complex with **20** (gold sticks, PDB 8I2N). (C) Superimposition of the co-crystal structures of RIPK1–**20** complex (green ribbons and gold sticks) and RIPK1–**5** complex (gray ribbons and sticks, PDB 4NEU). (D) Cartoon showing interactions between **20** and the ATP-binding pocket of RIPK1, key residues were shown as sticks, and H-bonds were indicated as red dashes. (E) The residue side chains of RIPK1 potentially interacting with **20** through van der Waals forces.

5-membered ring within **20** between the linker amide NH and the 2-nitrogen atom in the pyrazole ring.

Consistent with the binding mode, replacing the benzimidazole of **20** with an indole (**28**) or indazole (**29**) weakened the hinge H-bond and led to the loss of activity (Table 2). **27** was found to be more potent than **20**, especially against mRIPK1. Therefore, optimization efforts were then focused on the scaffold of **27**. As the *N*-methyl amide group of **27** appeared to protrude toward the solvent phase, more hydrophilic groups such as 2-(dimethylamino)ethyl (**30**), 2-(4-methylpiperazin-1-yl)ethyl (**31**) and 2-morpholinoethyl (**32**) were introduced into **27**. However, these analogs were less effective against mRIPK1. In contrast, introducing a hydrophobic methoxy group (**33**–**35**) considerably increased the potency against both hRIPK1 and mRIPK1 but caused cytotoxicity at high concentrations. Weakening the hinge H-bond of **34** resulted in a dramatic decrease in potency (**36**), and the quinazoline head (**37**) was also less potent than the benzamide head. We hypothesized that adding an H-bond donor in the head subunit of **27** could increase its potency. However, introducing a pyrrolopyrimidine head resulted in loss of activity (**38**). Inspired by the structure of ATP, we introduced an adenine head to **27** and discovered **39**, which had single-digit nanomolar or subnanomolar IC₅₀ values in both human and mouse cell models. Further modifications to the adenine head of **39** by changing the pyrimidine ring into a pyridine ring (**40**) or removing the H-bond acceptor (**41**) only decreased its potency. Consistently, introducing an adenine head to **21** provided a more potent inhibitor (**43**), and removing nitrogen atoms from the adenine of **43** (**44**–**46**) decreased its potency.

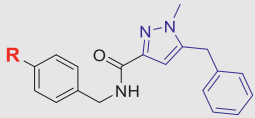
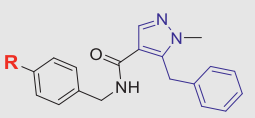
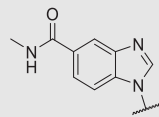
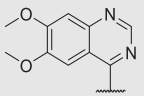
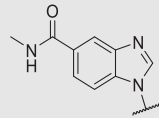
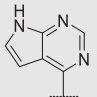
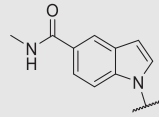
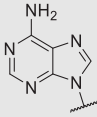
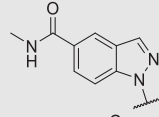
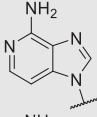
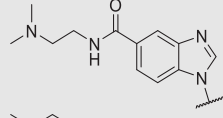
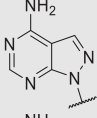
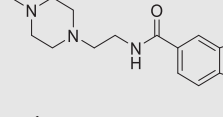
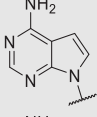
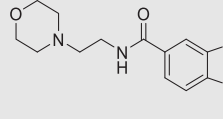
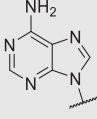
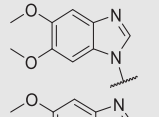
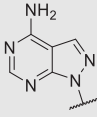
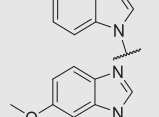
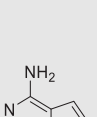
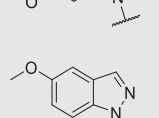
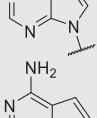
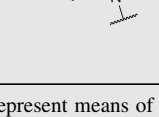
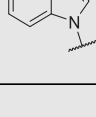

In this round of optimization, **39** exhibited extraordinary potency against both hRIPK1 and mRIPK1. To elucidate the SAR, we conducted a molecular docking study using the co-crystal structure of hRIPK1–**20** (Fig. 4). The results predicted a reliable binding mode for **39** that was highly similar to that of **20**, with a docking score of -13.6 . In this binding mode, the adenine head of **39** forms two H-bonds with Met95 in the hinge region of RIPK1 (Fig. 4A). The phenyl ring in the tail subunit of **39** is positioned exactly where that of **20** is located,

resulting in distinct orientation for the benzyl methylene (Fig. 4B). While the *N*-methyl of **39** occupies the same position as the methylene of **20** did, the methylene of **39** could interact with Ala155 of RIPK1 and contribute to stronger affinity. Compared to **20**, **43** shares the same head subunit as **39** but was less effective against mRIPK1. This indicated the sensitivity of mRIPK1 to be more dependent on the tail subunit of **39**. To investigate why this occurs, we compared the amino acid residue sequences of mouse and human RIPK1 (Fig. 4B). Most residues around the tail subunit of inhibitors are identical between both homologs; however, mRIPK1 has a DLGV-motif instead of hRIPK1's DLGL-motif, which could result in differences in sensitivity.

Based on **39**, we further studied the SAR of the tail subunit (Table 3). Consistent with those of **20**, larger *N*-substitution in the pyrazole ring led to a decrease in potency (**47**). To stabilize conformations favored by RIPK1 through an intramolecular H-bond similar to that of **20**, we introduced a 3-chloro to the scaffold of **39** and obtained **48** with comparable potency. Moreover, replacing the pyrazole ring with a 1,2,3-triazole ring led to a significant increase in potency (**49**). Docking results predicted a binding mode for **49** similar to that of **39** with an intramolecular H-bond and a docking score of -13.8 (Fig. 5A). Notably, removing the *N*-methyl from **49** resulted in a serious loss of potency. On the other hand, **51** with a bioisosteric 1-methyl-5-fluoro-1*H*-pyrrole ring showed comparable potency to **39**. However, analogs with larger substituents at 5-position (**52**, **53**) showed decreased potency.

In addition to optimizing the pyrazole tail of **39**, we also attempted to optimize its linker (Table 3). Our results showed that (*S*)-methylation of the linker methylene (**54**) further improved the potency of **39**, whereas (*R*)-methylation (**55**) or di-methylation (**56**) led to opposite effects. Combining the intramolecular H-bond with the (*S*)-methyl feature resulted in even stronger potency but also increased cytotoxicity at higher concentrations (**57**, **58**). Inspired by the bicyclic tail of **4** with more favorable

Table 2 Optimization of the head subunits (R) based on **20** and **27**^a.

		20 ⇒ 				27 ⇒ 					
		28, 29, 43-46				30-42					
Compd.	R	EC ₅₀ (nmol/L) ^b				Compd.	R	EC ₅₀ (nmol/L) ^b			
		FADD ^{-/-} Jurkat		L929				FADD ^{-/-} Jurkat		L929	
		TNFα	T+S	TNFα	T+S			TNFα	T+S	TNFα	T+S
20		5.1	44	312	2022	37		233	1503	n.d.	n.d.
27		0.5	5.2	20	77	38		152	747	>10,000	>10,000
28		>10,000	>10,000	>10,000	>10,000	39		0.04	1	0.9	3.6
29		>10,000	>10,000	>10,000	>10,000	40		0.3	2.3	1.2	6.3
30		53	368	>10,000	>10,000	41		0.4	6.9	9.9	23
31		0.01	0.6	5632	>10,000	42		4.2	8	0.1	0.9
32		0.5	3	32	190	43		0.06	0.3	25	384
33^c		0.02	0.1	0.06	0.4	44		71	451	6548	>10,000
34^c		0.002	0.1	0.005	0.08	45		137	980	2887	>10,000
35^c		0.01	0.6	0.03	0.4	46		361	>10,000	2316	>10,000
36		18	128	n.d.	n.d.	1		94	590	112	689
						2		0.5	3.9	1195	8279

^aData represent means of three replicates.^bCell viability assays, T = TNFα, S = SM164.^cWith cytotoxicity at high concentrations.

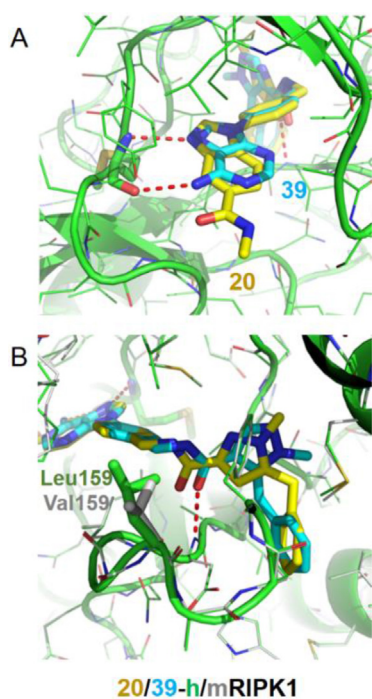


Figure 4 The predicted binding mode of **39** (azure sticks) based on the RIPK1-**20** (yellow sticks) co-crystal structure. The docking study predicted an additional H-bond (red dash) for **39** with the hinge region of RIPK1 (A), and similar but distinct interactions for the tail subunit of **39** compared to that of **20** (B). In panel B, the structure of mRIPK1 (gray ribbons and sticks) was aligned with that of hRIPK1 (green ribbons and sticks).

pharmacokinetic (PK) properties¹², we introduced a fused 6-membered ring to replace the pseudo-5-membered ring of **49**. The resulting compound, **59**, showed slightly weaker potency against mRIPK1 than its predecessor. Its 5,5-bicyclic analog, **60**, also exhibited weaker potency. In contrast, **61** with a bicyclic tail more similar to that of **4** had a much weaker effect against mRIPK1. After adding a (*S*)-methyl to **59** and **60**, we obtained **62** and **63** with cellular potencies between those of **39** and **49**. Docking results predicted **62** binds similarly to **49**, with a docking score of -14.587 (Fig. 5B). In this binding mode, the 6,5-bicyclic tail of **62** adopts a similar orientation to the pseudo-5,5-bicyclic tail of **49**. Additionally, the (*S*)-methyl of **62** potentially interacts with Leu159 of RIPK1 *via* hydrophobic effects, which could explain its increased potency. So far in the cellular assays, several of our inhibitors have shown significantly better potency against RIPK1—especially mRIPK1—compared to many reported RIPK1i.

The RIPK1i with outstanding cellular potency were further assessed for their stability in liver microsomes (Fig. 6A). **20** and **27**, which share the same benzamide head, showed good stability in both mouse or human liver microsomes (MLM/HLM), with half-lives ($t_{1/2}$) around 40 min. In contrast, **33** and **34** with more hydrophobic heads showed moderate stability in HLM and rather short $t_{1/2}$ s in MLM. Meanwhile, **39** with an adenine head showed good stability in both HLM and MLM. However, its close analogs with fewer nitrogen atoms, **40** and **42**, were significantly less stable. For the tail subunit, adding a chlorine (**48**) or one more nitrogen atom (**49**) to **39** remarkably improved the MLM stabilities, whereas the pyrrole tail (**51**) was much less stable.

Nevertheless, (*S*)-methylation (**54**) and cyclization (**62**, **63**) barely affected the stability of **39**.

Next, inhibitors that were stable in microsomes were selected for evaluation in an *in vitro* hRIPK1 kinase activity assay (Fig. 6B). In this assay, **1** and **2** were used as controls with IC_{50} values of 445 and 10.2 nmol/L, respectively. **39** was found to be comparably active to **2** with an IC_{50} of 9.5 nmol/L, while **49** and **54** were slightly more potent with IC_{50} values around 6 nmol/L. **62** was found to be threefold more potent than **2** against hRIPK1 *in vitro*, with an IC_{50} of 3.5 nmol/L. Meanwhile, **62** was at least 200-fold less potent against hRIPK3 with an IC_{50} of 730 nmol/L, while **39**, **49** and **54** were even weaker with IC_{50} values over 1 μ mol/L (Fig. 6B).

62 was then profiled against a diverse panel of 468 kinases using an *in vitro* ATP-site competition binding assay^{29,30} at a concentration of 100 nmol/L, and exhibited good overall selectivity among the kinome (Fig. 6C and Supporting Information Fig. S2). The profiling results suggested that RIPK1 was the top hit and that TRKA and DDR1/2 could potentially be off-targets for **62**. To assess the inhibitory effects of our RIPK1i against TRKA in cellular contexts, **62** and **63** were tested for their anti-proliferative abilities in engineered Ba/F3 cells whose proliferation is dependent on a TEL-TRKA fusion (Fig. S2A). The results showed that **62** was relatively weak against TRKA with an IC_{50} of 634 nmol/L, while **63** was almost inactive against TRKA ($IC_{50} > 1000$ nmol/L). On the other hand, reported siRNA screening results indicated that knockdown of neither TRKA nor DDR1/2 could affect the necroptotic pathway³¹, consistently, inhibition of DDR1/2 with a reported inhibitor³² showed no effect on necroptosis in cells (Fig. S2B).

These inhibitors were also preliminarily evaluated for potential drug–drug interactions and hepatotoxicity. In a panel of selected cytochrome P450 (CYP) enzymatic assays, they were inactive against most CYPs with IC_{50} values over 10 μ mol/L, except that **39** and **49** weakly inhibited CYP2C8 (Fig. 6D). At a concentration of 50 μ mol/L, these inhibitors showed negligible cytotoxic effects in the HepG2 human hepatocellular carcinoma cells compared to **1** and **2** (Fig. S2C). Additionally, these inhibitors were assessed for potential cardiotoxicity in a hERG safety assay, and all were found to be inactive with IC_{50} values over 30 μ mol/L (Fig. 6D). Overall, **62** demonstrated satisfactory selectivity for RIPK1 both *in vitro* and in cells.

To evaluate its inhibitory effects on the necroptotic signaling downstream of TNF α , **62** was titrated in FADD^{-/-} Jurkat and L929 cells stimulated with TNF α and SM164 (Fig. 7A). Western blot results showed that in the FADD^{-/-} Jurkat cells, **62** at 8 nmol/L was able to abolish the stimulated phosphorylation and activation of RIPK1 and MLKL, and eliminated most phosphorylation of RIPK3. In comparison, **2** was slightly weaker than **62**, and **1** was the least potent with effective concentrations at a sub-micromolar level. In L929 cells, **62** almost completely blocked the phosphorylation cascade at 40 nmol/L. In comparison, **1** at 1 μ mol/L showed similar effects whereas **2** became inactive even at 1 μ mol/L. **62** was also tested in the RIPK3-dimerization-induced necroptosis assay and showed no protective effects at all, confirming that RIPK1 is its sole target in the necroptotic pathway (Fig. 7B). On the other hand, **62** at 5 μ mol/L completely abolished the activation of RIPK1 in the human lung organoids infected with SARS-CoV-2, and exerted very strong antiviral effects compared to reported RIPK1i (Fig. 7C). Collectively, **62** potently and selectively inhibited the kinase activity of RIPK1 in various cell types.

Table 3 Optimization of the subunit R based on **39**^a.

39 \Rightarrow

47-63

Compd.	R	EC ₅₀ (nmol/L) ^b				Compd.	R	EC ₅₀ (nmol/L) ^b			
		FADD ^{-/-}		L929				FADD ^{-/-}		L929	
		Jurkat		Jurkat				Jurkat		Jurkat	
		TNFα	T + S	TNFα	T + S			TNFα	T + S	TNFα	T + S
39		0.04	1	0.9	3.6	56		7.5	28	550	6964
47		1.2	35	22	74	57^c		0.09	0.3	0.3	0.4
48		0.2	0.7	0.5	4.6	58^c		<0.01	<0.01	<0.01	<0.01
49		0.06	0.5	0.03	0.06	59		0.2	2.3	8.4	39
50		2.8	273	n.d.	n.d.	60		0.05	2.9	4.8	116
51		0.1	1.6	0.9	74	61		0.3	0.4	1390	2729
52		6.6	80.6	n.d.	n.d.	62		0.02	0.1	0.2	1.3
53		214	1860	875	3770	63		0.03	0.4	0.3	1.6
54		0.08	0.3	0.4	0.6	1		94	590	112	689
55		36	132	52	219	2		0.5	3.9	1195	8279

^aData represent means of three replicates.^bCell viability assays, T = TNFα, S = SM164.^cWith cytotoxicity at high concentrations.

To select a suitable inhibitor for animal studies, we evaluated the PK properties of selected inhibitors in mice following intravenous (iv) and oral (po) delivery (Table 4). **39**, **49**, **54**, and **63** showed overall comparable PK properties following an oral dose at 10 mg/kg (mpk). Their $t_{1/2s}$ ranged from 0.90 to 1.65 h, maximum concentrations (C_{max}) ranged from 714 to 1338 μg/L, area under the curve (AUC) values ranged from 1695 to 4110 μg h/L, and bioavailabilities ranged from 25.4% to 37.0%. In comparison, **48** at 10 mpk (po) showed more optimized PK properties with remarkably higher C_{max} , AUC, and bioavailability

parameters. **62** at 5 mpk (po) was even better with the longest $t_{1/2}$ (3.86 h) and the highest bioavailability (82.2%). Additionally, **62** showed a favorable PK profile in rats as well with a $t_{1/2}$ of 4.19 h, a C_{max} of 505 μg/L, an AUC of 2202 μg·h/L, and a bioavailability of 34.1% following an oral dose at 5 mpk (Table 4). Taken together, these results suggested that **62** is a more optimal choice for further animal studies.

In the end, we evaluated the efficacy and tolerability of **62** in mouse models of RIPK1-dependent acute or chronic inflammatory disease (Fig. 8). In a TNFα-induced systemic inflammatory

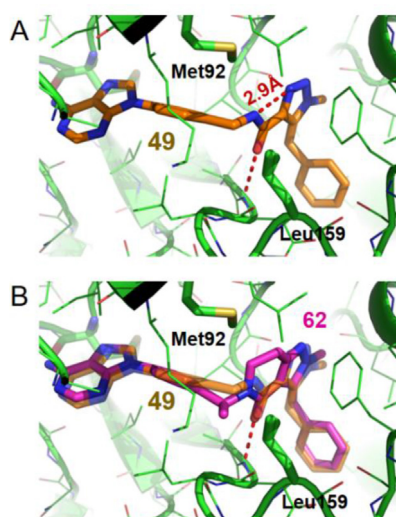


Figure 5 The predicted binding mode of **49** (orange sticks) and **62** (magenta sticks) based on the RIPK1-20 co-crystal structure, which indicates an intramolecular H-bond (red dash) in **49** (A) and a highly similar conformation for **62** (B).

response syndrome (SIRS) mouse model, **62** at 2 mpk (*po*) completely mitigated the acute hypothermia in mice and almost eliminated the symptoms even at the dose of 1 mpk (Fig. 8A). Furthermore, **62** at 1 mpk (*po*) protected all mice from the fatality while 6 out of 7 mice from the control group died of SIRS within 36 h. The pharmacodynamic study results showed that treatments with **62** at 1 mpk almost eliminated TNF α -induced activation of RIPK1 in mouse organs (Supporting Information Fig. S3). Meanwhile, the phosphorylation levels of the downstream effector, MLKL, were also significantly suppressed by treatments with **62** at 2 mpk (Supporting Information Fig. S4).

On the other hand, in a chronic IBD mouse model with adult-onset intestinal inflammation and splenomegaly based on a *Ripk1*^{K612R/K612R} knockin³³, we observed significantly reduced diarrhea and weight loss symptoms in mice orally dosed with **62** at 10 or 20 mpk per day (QD) for a continuous period of 40 days, compared to the control group (Fig. 8B). Notably, the colorectal stricture, splenomegaly, and thymus hyperplasia symptoms had been significantly alleviated in the *Ripk1*^{K612R/K612R} mice dosed with **62**, and no adverse effects had been observed in these mice during this long-term treatment (Supporting Information Fig. S5). Finally, in a RA mouse model induced by collagen antibodies and LPS¹³, daily oral administration of **62** at 15 or 30 mpk for 8 days could effectively eliminate most RA symptoms, including paw edema, erythema, and joint stiffness, without affecting the body-weight in mice (Fig. 8C and Supporting Information Fig. S6). These findings suggested that **62** is an orally bioavailable and tolerable RIPK1i that can effectively suppress RIPK1-dependent acute or chronic inflammations *in vivo*.

3. Conclusions

Despite being homologs and that both can be inhibited by type-II KI, RIPK1 and RIPK3 have very limited structural similarities in their hydrophobic pockets. So far only the pocket of RIPK1 has been proved utterly exploitable for selective targeting^{20,24}. The RIPK3i, **10**, was reportedly to be ineffective against mRIPK3²⁵, but in our

assays, it effectively protected mouse L929 cells from necroptosis, without inducing apoptosis like other RIPK3i. This indicates that its inhibitory mechanism is distinct from that of type-I RIPK3i. Nevertheless, modifications of **10** did generate moderately active dual inhibitors of RIPK1/3 with a typical type-II KI pharmacophore.

By utilizing ligands that are more specific to the hydrophobic pocket of RIPK1, we were able to further modify these moderate RIPK1/3 dual inhibitors and successfully obtained potent and selective type-II RIPK1 inhibitors. The co-crystal structure and molecular docking results showed clear interactions between these inhibitors and both the hinge region and the hydrophobic pocket of RIPK1, which facilitated our lead optimization process. Notably, our inhibitors rendered RIPK1 in DLG-out/Glu-out conformations as the selective type-III RIPK1i did, whereas typical type-II KIs usually adopt DLG-out/Glu-in binding modes, which could explain the good selectivity of our inhibitors. In addition, minor optimization of the tail subunit resulted in significant improvement in potency, especially against mRIPK1. The optimized lead, **62**, exhibited excellent potency against both human and mouse RIPK1 in cells with subnanomolar EC₅₀ values and hundredfold selectivity windows. It also showed stronger effects in suppressing the viral replication of SARS-CoV-2 in human lung organoids, compared to reported RIPK1i. With a favorable PK profile, low oral doses of **62** exerted incredible anti-inflammatory effects in various mouse models of acute or chronic inflammation mediated by RIPK1. In summary, **62** and its analogs provide useful probes for the pharmacological perturbation of RIPK1 in animal models and promising leads for clinical drug developments.

4. Experimental

4.1. Chemistry

The synthesis of **20** and **62** is outlined in Scheme 1. Other final compounds were prepared using similar procedures. Starting from the commercially available protected 4-iodobenzylamines (**64**) and benzimidazoles (**65**) or adenine (**66**), the intermediates **67** and **68** can be obtained by Ullmann coupling. After deprotection of **67** or **68**, the resulting benzylamines can be coupled with carboxylic acids (**69**) to form amides, directly producing **20** and its analogs. On the other hand, the arylamine **70** can be prepared with reported procedures and converted into aryl iodide **71** through diazotization³⁴. Suzuki–Miyaura coupling of **71** with an alkene boronic ester yields the enol ether **72**, which can be hydrolyzed to the aldehyde **73** under acidic conditions. The benzylamine resulting from deprotection of **68** can then be coupled with **73** through reductive amination, to provide the secondary amine intermediate **74**. Finally, intramolecular cyclization of **74** under Lewis acid catalysis produces **62** and its analogs with bicyclic tails.

Unless otherwise noted, reagents and solvents were obtained from commercial suppliers and were used without further purification. Reactions were run in round bottom flasks or glass vials and stirred with Teflon-coated magnetic stir bars. Solvent evaporation was performed on rotary evaporators under reduced pressure. Reactions were monitored by thin layer chromatography, LC–MS or UPLC/MS using water +0.05% formic acid (solvent A) and acetonitrile + 0.05% formic acid (solvent B). Preparative HPLC was performed on a C18 column (19 × 100 mm, 5 μ mol/L) using a gradient of 10%–95% acetonitrile in water containing 0.05% trifluoroacetic acid (TFA) over 10 min (15 min run time) at a flow rate of 15 mL/min. All final compounds are >95% pure as

determined by HPLC analysis. ^1H NMR (400 MHz) and ^{13}C NMR (101 MHz) spectra were recorded at ambient temperature in the specified deuterated solvents. Observed proton absorptions are reported as δ units of parts per million (ppm) relative to tetramethylsilane (δ 0.0). Multiplicities are reported: s (singlet), d (doublet), t (triplet), q (quartet), dd (doublet of doublets), and m (multiplet). Coupling constants are reported as a J value in Hertz (Hz).

tert-Butyl(4-(5-(methylcarbamoyl)-1H-benzof[*d*]imidazole-1-yl)benzyl)carbamate (**67**). **64A** (200 mg, 0.60 mmol), **65** (126 mg, 0.72 mmol), Cs_2CO_3 (390 mg, 1.20 mmol), cuprous iodide (57 mg, 0.30 mmol), 4,7-dimethoxy-1,10-phenanthroline (43 mg, 0.18 mmol) were stirred in DMSO (3.0 mL) and heated to 100 °C and stirred overnight under nitrogen protection. The reaction mixture was filtered and purified by reverse phase C18 column ($\text{CH}_3\text{CN}:\text{H}_2\text{O} = 0\text{--}80\%$) to afford compound **67** in 42% yield as a brown oil. ^1H NMR (400 MHz, chloroform-*d*) δ 8.22 (d, $J = 1.6$ Hz, 1H), 8.16 (s, 1H), 7.90–7.79 (m, 1H), 7.56–7.46 (m, 5H), 6.27 (s, 1H), 5.01 (s, 1H), 4.43 (d, $J = 6.2$ Hz, 2H), 3.08 (d, $J = 4.8$ Hz, 3H), 1.49 (s, 9H). UPLC–MS (ESI) calculated for $\text{C}_{21}\text{H}_{24}\text{N}_4\text{O}_3$ [$\text{M} + \text{H}$] $^+$: 380.2, found: 381.1.

1-(4-((5-Benzyl-1-methyl-1H-pyrazole-3-carboxamido)methyl)phenyl)-N-methyl-1H-benzof[*d*]imidazole-5-carboxamide (**20**). To a solution of **67** (203 mg, 0.53 mmol) in CH_2Cl_2 (5.0 mL) was

added TFA (1.0 mL). The reaction mixture was stirred at room temperature for 3 h, then the solution was diluted with CH_2Cl_2 and evaporated *in vacuo* several times to remove TFA. The crude material was used for the next step without further purification.

To a stirred suspension of **69** (15 mg, 0.07 mmol), HATU (32 mg, 0.09 mmol), and DIEA (23 mg, 0.18 mmol) in CH_2Cl_2 (2.0 mL) were added the above-mentioned product (20 mg, 0.07 mmol). The reaction mixture was stirred at room temperature for 4 h. The solution was diluted with CH_2Cl_2 and partitioned between CH_2Cl_2 (10 mL) and water (5 mL). The organic layer was washed by brine and dried over Na_2SO_4 , then evaporated *in vacuo* and the residue was purified by silica gel column chromatography ($\text{CH}_3\text{OH}:\text{CH}_2\text{Cl}_2 = 0\text{--}20\%$) to afford compound **20** in 59% yield as a white solid. ^1H NMR (400 MHz, $\text{DMSO}-d_6$) δ 8.85 (s, 1H), 8.77 (t, $J = 6.4$ Hz, 1H), 8.55 (d, $J = 4.5$ Hz, 1H), 8.31 (d, $J = 1.1$ Hz, 1H), 7.91–7.86 (m, 1H), 7.72–7.63 (m, 3H), 7.56 (t, $J = 9.3$ Hz, 2H), 7.34 (t, $J = 7.3$ Hz, 2H), 7.28–7.22 (m, 3H), 6.37 (d, $J = 1.7$ Hz, 1H), 4.49 (t, $J = 5.7$ Hz, 2H), 4.07 (s, 2H), 3.78 (s, 3H), 2.80 (dd, $J = 14.9, 4.5$ Hz, 3H). HRMS (ESI) calculated for $\text{C}_{28}\text{H}_{26}\text{N}_6\text{O}_2$ [$\text{M} + \text{H}$] $^+$: 478.2117, found: 479.2182.

Ethyl 5-benzyl-3-iodo-1-methyl-1H-pyrazole-4-carboxylate (**71**). $\text{Con. H}_2\text{SO}_4$ (265 mg, 2.7 mmol) was added dropwise to the solution of **70** (350 mg, 1.35 mmol) in $\text{MeCN}/\text{H}_2\text{O}$ (3 mL/6 mL), stirred at 0 °C for 10 min. Sodium nitrite (102 mg, 1.48 mmol) in H_2O (3.0 mL)

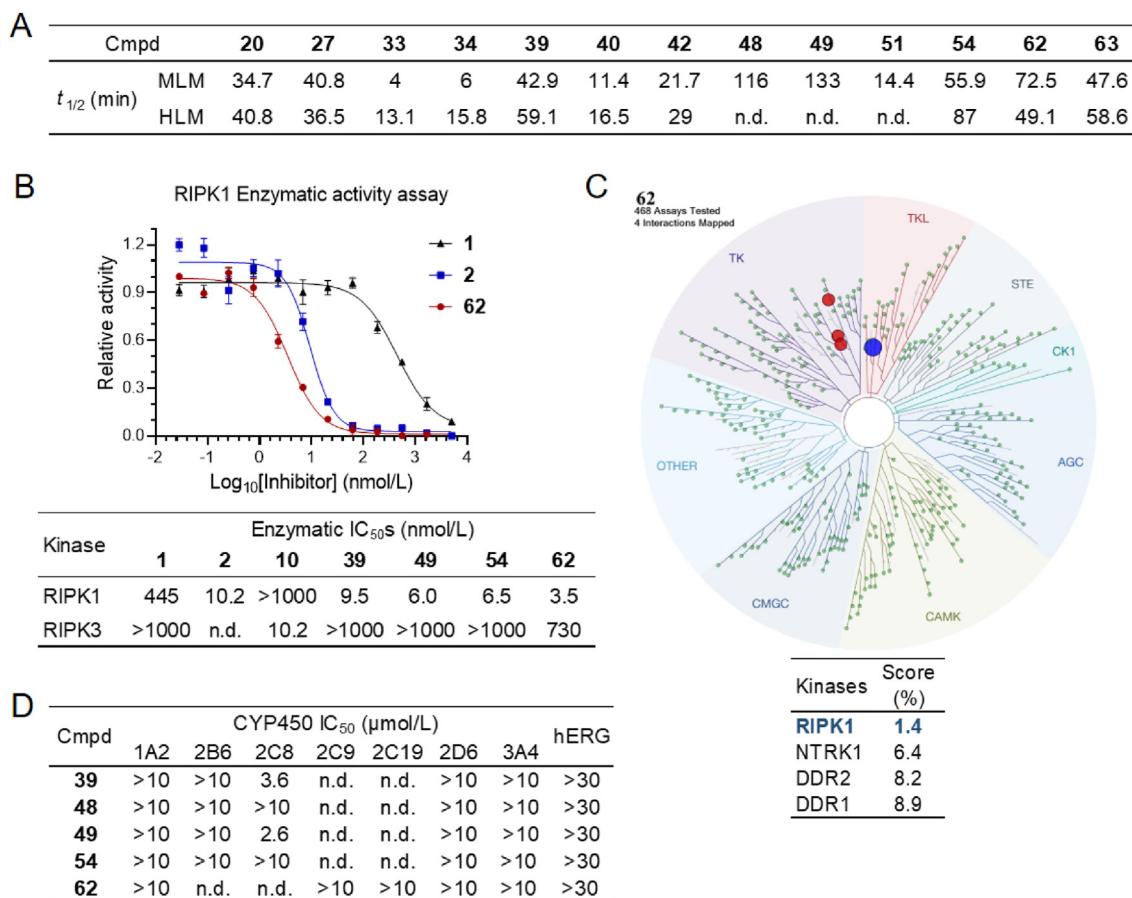


Figure 6 *In vitro* characterization of lead compounds. (A) Metabolic stability of selected RIPK1i in MLM and HLM. (B) Representative inhibition curves and IC_{50} values for lead compounds against hRIPK1 or hRIPK3 based on enzymatic assays. (C) Kinase selectivity profiles for **62** at 100 nmol/L against a diverse panel of 468 kinases. Scores for primary screen hits are reported as a percent of the DMSO control (% control), and the lower score indicated a higher probability of being a hit. (D) IC_{50} values for lead compounds against a panel of CYPs and hERG. Data represent means of three replicates; n.d., not detected.

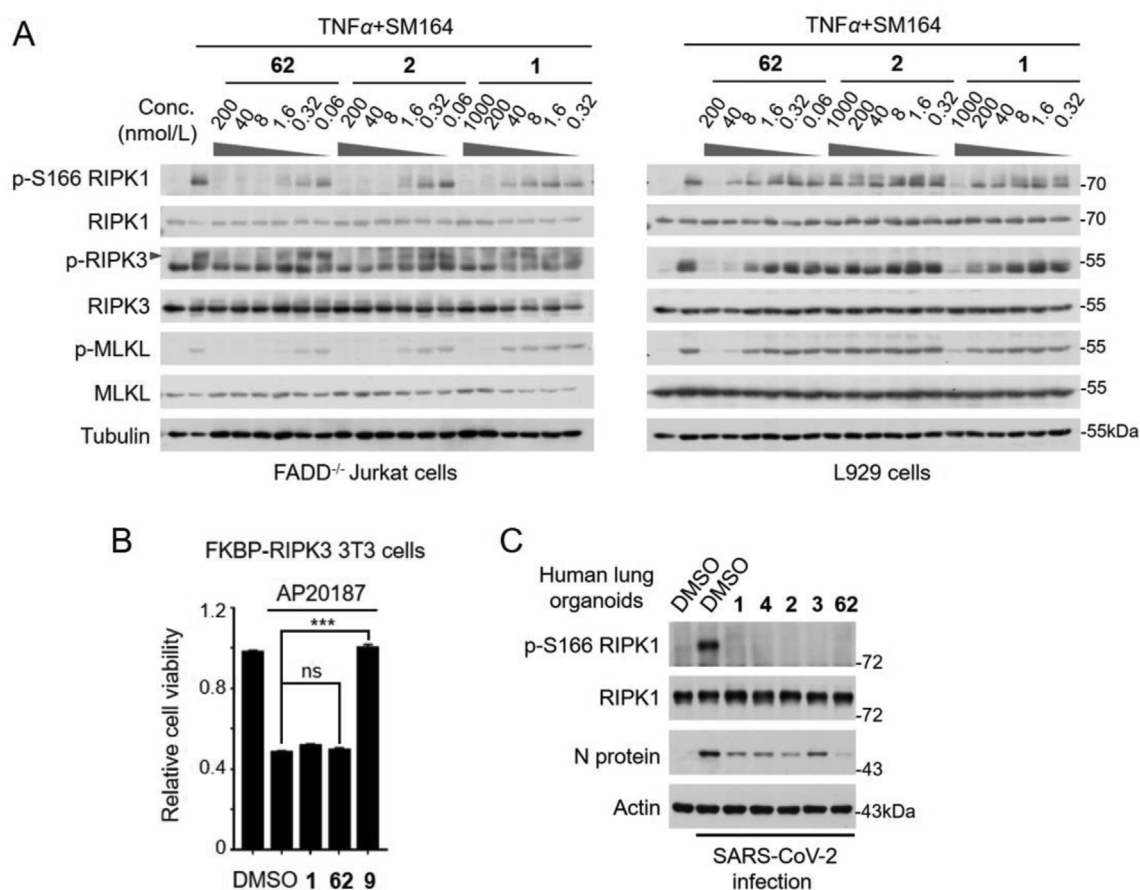


Figure 7 Interrogating RIPK1 in cellular models with **62**. (A) Human FADD^{-/-} Jurkat or mouse L929 cells were treated with TNF α (40 ng/mL) and SM164 (25 nmol/L) for 15 h in the presence of **1**, **2**, or **62** at indicated concentrations, then lysed and followed by Western blotting analysis using species-specific antibodies. (B) Bar graph showing the anti-necroptotic effects of each compound at 10 μ mol/L in mouse 3T3 cells engineered with an FKBP-RIPK3-fusion. Cells were treated with the FKBP-dimerizing agent, AP20187 (100 nmol/L), in the presence of DMSO or compounds for 15 h before the viability test. Data represent means \pm SD ($n = 3$); $^{**}P < 0.01$, $^{***}P < 0.001$, unpaired Student's t -test. (C) Human lung organoids were infected with SARS-CoV-2 (0.3 MOI) for 1 h, then washed out with PBS and cultured with normal medium and indicated compounds (5 μ mol/L) for an additional 48 h, then lysed and followed by Western blotting analysis. The viral loads of SARS-CoV-2 were indicated by its N protein levels.

was added dropwise to the solution and stirred at 0 $^{\circ}$ C for 1 h, then potassium iodide (672 mg, 4.05 mmol) was added slowly to the mixture and stirred at 0 $^{\circ}$ C for another 1 h before quenched by sodium thiosulfate solution. The solution was diluted with ethyl acetate and partitioned between ethyl acetate (60 mL) and water (10 mL). The organic layer was washed by H₂O and brine, dried over Na₂SO₄, then evaporated *in vacuo* and the residue was purified by silica gel column chromatography (EA:PE = 0–50%) to afford compound **71** in 30% yield as a yellow solid. ¹H NMR (400 MHz, DMSO-*d*₆) δ 7.29 (dd, $J = 8.2, 6.5$ Hz, 2H), 7.25–7.19 (m, 1H), 7.14–7.03 (m, 2H), 4.42 (s, 2H), 4.32 (q, $J = 7.1$ Hz, 2H), 3.71 (s, 3H), 1.33 (t, $J = 7.1$ Hz, 3H). LC-MS (ESI) calculated for C₁₄H₁₅IN₂O₂ [M + H]⁺: 370.0, found: 370.1.

Ethyl (E)-5-benzyl-3-(2-ethoxyvinyl)-1-methyl-1H-pyrazole-4-carboxylate (72). **71** (150 mg, 0.41 mmol), (*E*)-1-ethoxyethene-2-ylboronic acid pinacol ester (161 mg, 0.81 mmol), Pd(dppf)Cl₂ (30 mg, 0.04 mmol), Cs₂CO₃ (294 mg, 0.90 mmol), were stirred in DME/H₂O (2.0 mL/0.4 mL) and heated at 90 $^{\circ}$ C, stirred overnight under nitrogen protection. The reaction mixture was filtered and purified by reverse phase C18 column (CH₃CN:H₂O = 10%–100%) to afford compound **72** in 87% yield as a brown solid. ¹H NMR (400 MHz, chloroform-*d*) δ 7.37 (s, 0.5H), 7.34 (s, 0.5H), 7.28 (dd,

$J = 9.7, 2.6$ Hz, 2H), 7.20 (t, $J = 7.2$ Hz, 1H), 7.13–7.07 (m, 2H), 6.33 (d, $J = 13.0$ Hz, 1H), 4.38 (s, 2H), 4.27 (q, $J = 7.1$ Hz, 2H), 3.94 (q, $J = 7.0$ Hz, 2H), 3.64 (s, 3H), 1.35 (t, $J = 7.1$ Hz, 3H), 1.29 (t, $J = 7.1$ Hz, 3H). UPLC-MS (ESI) calculated for C₁₈H₂₂N₂O₃ [M + H]⁺: 314.2, found: 315.0.

Ethyl 5-benzyl-1-methyl-3-(2-oxoethyl)-1H-pyrazole-4-carboxylate (73). 6 N HCl (1.5 mL) was added to **72** (112 mg, 0.36 mmol) in THF (2.0 mL) at 0 $^{\circ}$ C, then the reaction was warmed to room temperature and stirred overnight. The solution was diluted with ethyl acetate and partitioned between ethyl acetate (15 mL) and water (5 mL). The organic layer was washed by NaHCO₃ saturated solution and brine, dried over Na₂SO₄, then evaporated *in vacuo*, and the crude product was used for the next step without further purification.

tert-Butyl (S)-1-(4-(6-amino-9H-purin-9-yl)phenyl)ethylcarbamate (68). **64B** (1.62 g, 4.66 mmol), Cs₂CO₃ (2.39 g, 7.34 mmol), cuprous iodide (444 mg, 2.33 mmol), 4,7-dimethoxy-1,10-phenanthroline (112 mg, 0.47 mmol) were stirred in DMSO (25.0 mL) and heated at 100 $^{\circ}$ C and stirred overnight under nitrogen protection. The reaction mixture was filtered and purified by reverse phase C18 column (CH₃CN:H₂O = 0–80%) to afford compound **68** in 39% yield as a yellow-white solid. ¹H NMR (400 MHz, chloroform-*d*) δ 8.42 (s, 1H), 8.06 (s, 1H), 7.70–7.59 (m, 2H), 7.51

Table 4 PK parameters of optimized RIPK1^a.

Compd.	Route	$t_{1/2}$	T_{max}	C_{max}	AUC_{0-t}	AUC_{0-inf}	CL	MRT _{0-inf}	V_{ss}	F
		(h)	(h)	($\mu\text{g/L}$)	($\text{h} \cdot \mu\text{g/L}$)	($\text{h} \cdot \mu\text{g/L}$)				
39^b	<i>po</i>	1.34	0.33	1338	2190	2210		2.55		25.4
	<i>iv</i>	0.81			862	882	1.1	2.08	2.35	
48^b	<i>po</i>	1.39	0.42	3053	8276	8395		4.05		63.9
	<i>iv</i>	0.81			1295	1314	0.8	1.97	1.55	
49^b	<i>po</i>	1.65	0.67	1218	4110	4334		5.75		33.3
	<i>iv</i>	1.03			1235	1415	0.7	10.50	6.98	
54^b	<i>po</i>	0.90	0.50	1200	2437	2485		3.05		37.0
	<i>iv</i>	0.44			659	672	1.5	1.98	2.98	
62^c	<i>po</i>	3.86	0.50	1977	6501	6517		2.81		82.2
	<i>iv</i>	1.29			471	476	0.6	1.49	0.94	
63^b	<i>po</i>	1.05	0.67	714	1695	1726		2.75		26.4
	<i>iv</i>	0.61			643	644	1.6	0.97	1.60	
62^d	<i>po</i>	4.19	0.50	505	2202	2253		6.82		34.1
	<i>iv</i>	0.91			390	397	0.8	1.03	0.77	

^aData represent means of three replicates.^bMice administered at 10 mpk (*po*) or 1 mpk (*iv*).^cMice or.^drats administered at 5 mpk (*po*) or 0.5 mpk (*iv*).

(d, $J = 8.1$ Hz, 2H), 5.87 (s, 2H), 4.96–4.86 (m, 1H), 1.96 (s, 1H), 1.48 (d, $J = 6.8$ Hz, 3H), 1.44 (s, 9H). UPLC–MS (ESI) calculated for $\text{C}_{18}\text{H}_{22}\text{N}_6\text{O}_2$ $[\text{M} + \text{H}]^+$: 354.2, found: 355.1.

Ethyl(S)-3-(2-((1-(4-(6-amino-9H-purin-9-yl)phenyl)ethyl)amino)ethyl)-5-benzyl-1-methyl-1H-pyrazole-4-carboxylate (74). To a solution of **68** (1.45 g, 4.08 mmol) in CH_2Cl_2 (20.0 mL) was added TFA (2.0 mL). The reaction mixture was stirred at room temperature for 4 h, then the reaction solution was diluted with CH_2Cl_2 and evaporated *in vacuo* for several times to remove TFA. The crude material was used for the next step without further purification.

To a stirred suspension of the above-mentioned product (1.1 g, 4.2 mmol), **73** (1.7 mmol) in DCE/DMF (10.0 mL/2.0 mL) were added acetic acid (306 mg, 5.1 mmol). The reaction mixture was stirred at room temperature for 30 min then added sodium triacetoxyborohydride (899 mg, 4.2 mmol) to the mixture, and stirred overnight at room temperature. DCE was evaporated *in vacuo*, the residue was filtered and purified by reverse phase C18 column ($\text{CH}_3\text{CN}:\text{H}_2\text{O} = 10\%–100\%$) to afford compound **74** in 66% yield as a yellow foam. ^1H NMR (400 MHz, chloroform-*d*) δ 8.43 (s, 1H), 8.06 (s, 1H), 7.65–7.50 (m, 4H), 7.27 (t, $J = 3.7$ Hz, 3H), 7.20

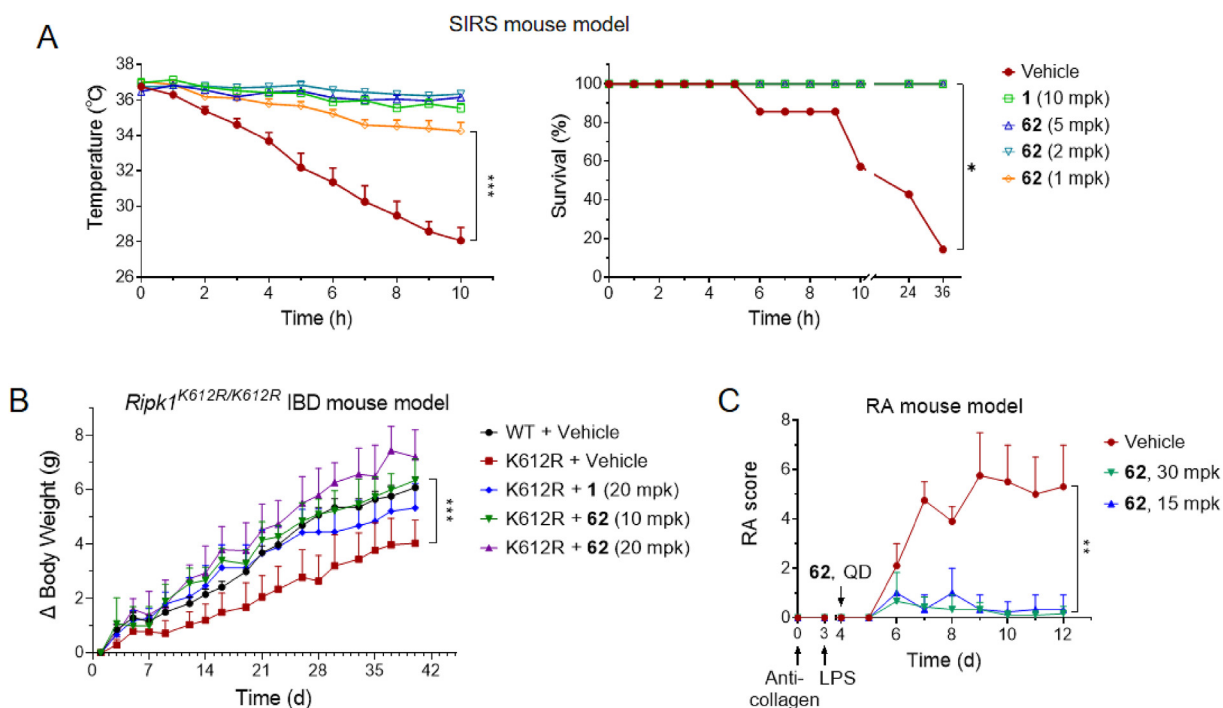
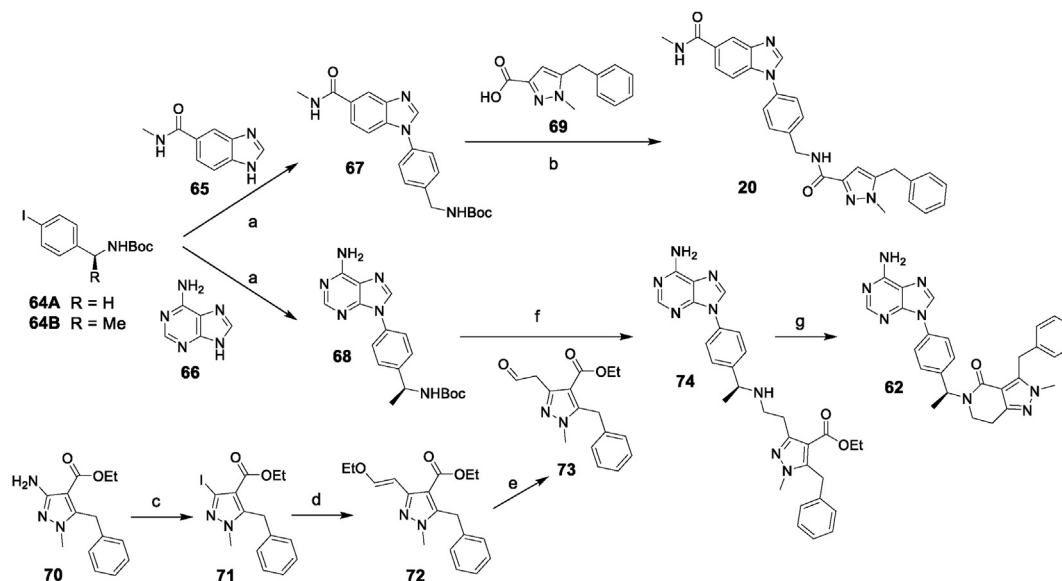


Figure 8 The anti-inflammatory effects of **62** *in vivo*. (A) Evaluation of **62** (*po*) in TNF α (10 μg) induced SIRS mouse model measuring reduction in body temperature and survival rates ($n = 7$). (B) Quantification of the bodyweight for each group of *Ripk1^{K612R/K612R}* mice treated with vehicle, **1** or **62** (*po*) ($n = 4$). (C) Quantification of the RA symptoms induced by collagen antibodies and LPS for each group of mice treated with vehicle or **62** (*po*) ($n = 3$). Data represent means \pm SD; ** $P < 0.01$, *** $P < 0.001$, paired Student's *t*-test.



Scheme 1 Reagents and conditions: (a) CuI, Cs₂CO₃, 4,7-dimethoxy-1,10-phenanthroline, DMSO, 100 °C, under N₂; (b) (1) TFA, CH₂Cl₂, (2) HATU, DIEA, CH₂Cl₂/DMF; (c) H₂SO₄, NaNO₂, CH₃CN/H₂O, 0 °C, then KI, 0 °C; (d) (*E*)-1-ethoxyethene-2-ylboronic acid pinacol ester, Pd(dppf)Cl₂, Cs₂CO₃, DME/H₂O, 90 °C, under N₂; (e) 6 N HCl, THF, 0 °C to rt; (f) NaBH(OAc)₃, AcOH, DCE/DMF, rt; (g) AlMe₃, xylene, 120 °C, under N₂.

(t, *J* = 7.3 Hz, 1H), 7.14–7.04 (m, 2H), 5.74 (s, 2H), 4.37 (s, 2H), 4.24 (q, *J* = 7.1 Hz, 2H), 3.93 (q, *J* = 6.5 Hz, 1H), 3.65 (s, 3H), 3.07 (t, *J* = 6.8 Hz, 2H), 2.96–2.75 (m, 2H), 1.37 (d, *J* = 6.4 Hz, 3H), 1.26 (t, *J* = 7.0 Hz, 3H). UPLC–MS (ESI) calculated for C₂₉H₃₂N₈O₂ [M + H]⁺: 524.3, found: 525.2.

(*S*)-5-(1-(4-(6-Amino-9H-purin-9-yl)phenyl)ethyl)-3-benzyl-2-methyl-2,5,6,7-tetrahydro-4H-pyrazolo[4,3-*c*]pyridin-4-one (**62**). Trimethylaluminium (1.5 mmol) was added dropwise to the solution of **74** (262 mg, 0.5 mmol) in dry xylene (20.0 mL), then heated to 120 °C and stirred overnight under nitrogen protection. The reaction was quenched by potassium sodium tartrate solution, then partitioned between ethyl acetate (60 mL) and water (20 mL). The organic layer was washed by brine, dried over Na₂SO₄, then evaporated *in vacuo* and the residue was purified by silica gel column chromatography (CH₃OH:CH₂Cl₂ = 0–20%) to afford compound **62** in 44% yield as a white solid. ¹H NMR (400 MHz, DMSO-*d*₆) δ 8.59 (s, 1H), 8.21 (s, 1H), 7.98–7.76 (m, 2H), 7.55 (d, *J* = 8.4 Hz, 2H), 7.43 (s, 2H), 7.37–7.27 (m, 4H), 7.26–7.16 (m, 1H), 6.01 (q, *J* = 7.0 Hz, 1H), 4.48–4.32 (m, 2H), 3.64 (s, 3H), 3.55–3.46 (m, 1H), 3.18–3.09 (m, 1H), 2.82–2.66 (m, 2H), 1.58 (d, *J* = 7.1 Hz, 3H). ¹³C NMR (101 MHz, DMSO-*d*₆) δ 162.65, 150.54, 149.66, 148.13, 145.28, 143.15, 142.97, 142.33, 137.56, 132.47, 128.65, 128.39, 128.16, 126.50, 124.12, 118.94, 110.02, 48.44, 41.42, 36.14, 29.00, 22.32, 16.45. HRMS (ESI) calculated for C₂₇H₂₆N₈O [M + H]⁺: 478.2230, found: 479.2303.

N-(4-(6-Amino-9H-purin-9-yl)benzyl)-5-benzyl-1-methyl-1H-pyrazole-4-carboxamide (**39**). The title compound was obtained as described in the general procedure (white solid). ¹H NMR (400 MHz, DMSO-*d*₆) δ 8.76–8.66 (m, 2H), 8.35 (s, 1H), 7.99 (s, 1H), 7.82–7.77 (m, 2H), 7.52 (d, *J* = 8.6 Hz, 2H), 7.31–7.25 (m, 2H), 7.21–7.17 (m, 3H), 4.51 (d, *J* = 5.8 Hz, 2H), 4.46 (s, 2H), 3.66 (s, 3H). ¹³C NMR (101 MHz, DMSO-*d*₆) δ 162.65, 150.54, 149.66, 148.13, 145.28, 143.15, 142.97, 142.33, 137.56, 132.47, 128.65, 128.39, 128.16, 126.50, 124.12, 118.94, 110.02, 48.44, 41.42, 36.14,

29.00, 22.32, 16.45. HRMS (ESI) calculated for C₂₄H₂₂N₈O [M + H]⁺: 438.1917, found: 439.1993.

N-(4-(6-Amino-9H-purin-9-yl)benzyl)-5-benzyl-3-chloro-1-methyl-1H-pyrazole-4-carboxamide (**48**). The title compound was obtained as described in the general procedure (white solid). ¹H NMR (400 MHz, DMSO-*d*₆) δ 8.50 (s, 1H), 8.45 (t, *J* = 6.0 Hz, 1H), 8.14 (s, 1H), 7.83–7.69 (m, 2H), 7.49–7.38 (m, 2H), 7.35 (s, 2H), 7.23 (dd, *J* = 8.0, 6.6 Hz, 2H), 7.18–7.07 (m, 3H), 4.44 (d, *J* = 6.0 Hz, 2H), 4.22 (s, 2H), 3.59 (s, 3H). ¹³C NMR (101 MHz, DMSO-*d*₆) δ 161.69, 152.55, 148.50, 148.10, 144.96, 141.95, 139.85, 136.97, 134.68, 132.77, 128.69, 128.27, 126.63, 123.59, 119.12, 113.10, 42.05, 36.78, 29.37. HRMS (ESI) calculated for C₂₄H₂₁ClN₈O [M + H]⁺: 472.1527, found: 473.1600.

N-(4-(6-Amino-9H-purin-9-yl)benzyl)-5-benzyl-1-methyl-1H-1,2,3-triazole-4-carboxamide (**49**). The title compound was obtained as described in the general procedure (white solid). ¹H NMR (400 MHz, DMSO-*d*₆) δ 9.30 (t, *J* = 6.3 Hz, 1H), 8.71 (s, 1H), 8.35 (s, 1H), 7.83–7.70 (m, 2H), 7.55 (d, *J* = 8.3 Hz, 2H), 7.37–7.26 (m, 2H), 7.27–7.14 (m, 3H), 7.18–7.07 (m, 3H), 4.54 (d, *J* = 6.3 Hz, 2H), 4.47 (s, 2H), 3.90 (s, 3H). ¹³C NMR (101 MHz, DMSO-*d*₆) δ 161.07, 153.14, 148.91, 148.61, 141.61, 139.99, 138.41, 138.24, 136.65, 132.90, 128.77, 128.44, 128.32, 126.78, 123.58, 119.12, 41.53, 34.67, 27.40. HRMS (ESI) calculated for C₂₃H₂₁N₉O [M + H]⁺: 439.1869, found: 440.1944.

(*S*)-*N*-(1-(4-(6-Amino-9H-purin-9-yl)phenyl)ethyl)-5-benzyl-1-methyl-1H-pyrazole-4-carboxamide (**54**). The title compound was obtained as described in the general procedure (white solid). ¹H NMR (400 MHz, DMSO-*d*₆) δ 8.55 (s, 1H), 8.48 (d, *J* = 7.9 Hz, 1H), 8.19 (s, 1H), 8.08 (s, 1H), 7.86–7.74 (m, 2H), 7.60–7.51 (m, 2H), 7.41 (s, 2H), 7.27 (dd, *J* = 8.0, 6.8 Hz, 2H), 7.20–7.12 (m, 3H), 5.20 (p, *J* = 7.2 Hz, 1H), 4.56–4.22 (m, 2H), 3.65 (s, 3H), 1.50 (d, *J* = 7.1 Hz, 3H). ¹³C NMR (101 MHz, DMSO-*d*₆) δ 162.31, 156.33, 153.12, 149.19, 144.68, 143.36, 139.67, 137.81, 137.53, 133.49, 128.51, 128.21, 127.02, 126.28, 123.03, 119.22,

114.46, 47.46, 36.31, 28.82, 22.33. HRMS (ESI) calculated for $C_{25}H_{24}N_8O$ $[M + H]^+$: 452.2073, found: 453.2147.

(*S*)-5-(1-(4-(6-Amino-9H-purin-9-yl)phenyl)ethyl)-3-benzyl-2-methyl-5,6-dihydropyrrolo[3,4-*c*]pyrazol-4(2H)-one (**63**). The title compound was obtained as described in the general procedure (white solid). 1H NMR (400 MHz, DMSO- d_6) δ 8.70 (s, 1H), 8.35 (s, 1H), 7.85–7.79 (m, 2H), 7.54 (d, $J = 8.3$ Hz, 2H), 7.32 (d, $J = 5.7$ Hz, 4H), 7.26–7.19 (m, 1H), 5.51 (q, $J = 7.1$ Hz, 1H), 4.44 (d, $J = 16.3$ Hz, 1H), 4.19 (s, 2H), 4.06 (d, $J = 16.3$ Hz, 1H), 3.79 (s, 3H), 1.65 (d, $J = 7.2$ Hz, 3H). ^{13}C NMR (101 MHz, DMSO- d_6) δ 163.38, 157.19, 152.94, 148.65, 148.56, 142.19, 141.68, 137.93, 137.25, 133.14, 128.77, 128.42, 127.79, 126.70, 123.81, 119.11, 115.48, 48.88, 41.58, 36.75, 29.51, 18.07. HRMS (ESI) calculated for $C_{26}H_{24}N_8O$ $[M + H]^+$: 464.2073, found: 465.2148.

4.2. Reagents

Cell lines were cultured as follows: L929 and NIH-3T3 cells were cultured in DMEM supplemented with 10% (*v/v*) FBS; Jurkat and Ba/F3 cells were cultured in RPMI-1640 with 10% FBS; HT-29 was cultured in McCoy's 5A with 10% FBS; HepG2 was cultured in MEM with 10% FBS; All the cells were maintained at 37 °C and 5% CO₂. All culture media and FBS were GIBCO™ and purchased from ThermoFisher (Waltham, MA, USA), common reagents were purchased from Sigma–Aldrich (Burlington, MA, USA) unless otherwise specified. The following commercial reagents were used in this study: TNF α (Novoprotein, Shanghai, China), mTNF α (Cell Sciences, Newburyport, MA, USA), monoclonal anti-collagen antibodies cocktail (Chondrex, Woodinville, USA). The following antibodies were used in this study: p-S345-MLKL (ab196436, mouse-specific), p-S358-MLKL (ab187091, human-specific), MLKL (ab172868, mouse-specific), MLKL (ab189612, human-specific) and RIPK3 (ab72106, human-specific) were purchased from Abcam (Cambridge, UK); RIPK1 (3493), p-S166-RIPK1 (31122, human-specific), p-T231/S232-RIPK3 (57220, mouse-specific) and p-S227-RIPK3 (93654, human-specific) were purchased from Cell Signaling Technology (Danvers, MA, USA); RIPK3 (AHP1797, mouse-specific) was purchased from BIO-RAD (Hercules, CA, USA); β -actin (I10813) and tubulin (I11107) were purchased from TransGen (Beijing, China); SARS-CoV-2 N protein (40588-T62) was purchased from Sino Biological (Beijing, China); p-S166-RIPK1 (mouse specific) was purchased from Biolyinx (Hangzhou, China). Chemical probes were purchased from Selleck (Shanghai, China) or prepared according to the literature.

4.3. Co-crystal structure determination and molecular docking

The expression, purification, and co-crystallization of recombinant RIPK1 protein (1-294, C34A, C127A, C233A, C240A) were following the reported procedures and conditions¹⁶. Diffraction datasets were collected at the beamline BL17U1 of the Shanghai Synchrotron Radiation Facility (Shanghai, China). The diffraction data sets were processed with the XDS program and the autoPROC suite^{35–37}. The initial phase for the complex structure was solved by molecular replacement using the PDB entry 4ITH as the search model with the program Phaser³⁸. The structural model was further manually re-built in Coot and refined with Phenix^{39,40}. The qualities of the final models were validated by MolProbity⁴¹ and listed in Supporting Information Table S1. The docking studies were performed based on coordinates of RIPK1-20 (PDB 8I2N)

using Schrödinger 2021 software suites (Schrödinger, New York, NY, USA)⁴². The best ligand poses were chosen based on the docking score, and scores of –10 or lower usually represent very good binding. All the structural figures were prepared in the program PyMol (Schrödinger).

4.4. In vitro profiling assays

The RIPK1 kinase activities were tested using a commercially available assay kit from Promega (Madison, Wisconsin, USA), and the RIPK3 kinase activities were tested similarly except that recombinant RIPK3 other than RIPK1 protein was used (SignalChem, Richmond, BC, Canada). The KINOMEScan assays were done by DiscoverX (Fremont, CA, USA), and the scores were reported as a percent of DMSO control, with the lower score usually indicating a higher probability of being a hit^{29,30}. The assays for microsomal stability, CYP450 inhibition and hERG inhibition were performed according to the literature^{43–45}.

4.5. Cell viability assays

The cells were plated at a density of 2000 (adherent) or 10,000 (suspended) cells per well in a 384-well white plate and incubated with DMSO or inhibitors. For necroptosis cell models, the cells were treated with inhibitors for 30 min before TNF α stimulation (10 ng/mL with 25 nmol/L SM164, or 40 ng/mL without SM164), then analyzed for viabilities 16 h after the stimulation. For cytotoxicity assessment, cells were treated with inhibitors for 72 h before viability analysis. The relative cell viabilities were determined using the Cell Titer Glo assay (Promega) and reported as percentages of the DMSO controls.

4.6. Immunoblotting analyses

HT29 or L929 cells were seeded in 6-well plates at a density of 4×10^5 cells per well 24 h before experiment. FADD^{-/-} Jurkat cells were seeded in 6-well plates at a density of 2×10^6 cells per well. Cells were pretreated with inhibitors for 1 h before applying stimulations. The human lung organoids infected with SARS-CoV-2 were prepared according to literature³, and treated with inhibitors for 48 h before being lysed. The whole-cell lysates were collected with 1% SDS lysis buffer (1% SDS, 150 mmol/L NaCl, 50 mmol/L Tris-HCl (pH 7.4)), and then boiled at 95 °C for 10 min. Total protein concentration was analyzed by BCA kit (ThermoFisher) and aligned with lysis buffer. Lysates were mixed with an equal volume of 2X loading buffer (100 mmol/L Tris-HCl (pH 6.8), 4% SDS, 20% glycerol, bromophenol blue, and 5% β -mercaptoethanol) and boiled at 95 °C for 10 min, then separated in 10% polyacrylamide gel electrophoresis. Protein was transferred onto 0.2 μ m nitrocellulose membrane and blotted with specific antibodies as indicated.

4.7. In vivo studies

For PK studies, male ICR mice or SD rats were dosed *via* tail vein (iv, 10% *v/v* DMA, 10% *w/v* Solutol HS 15 in normal saline at a dose of 0.5 or 1 mpk) or oral gavage (*po*, 3% *v/v* DMSO, 97% *v/v* aqueous HP- β -CD solution (30% *w/v*) at a dose of 10 or 5 mpk). Blood samples were collected at 5, 15, 30, 60, 120, 240, 360, 480, 720 and 1440 min (iv) and 15, 30, 60, 120, 240, 360, 480, 720 and 1440 min (*po*). The animal was restrained manually at the

designated time points, and approximately 30–50 μL of blood sample was collected *via* the retro-orbital plexus into tubes with EDTA2K. Plasma samples were separated by centrifugation of whole blood and stored below $-80\text{ }^{\circ}\text{C}$ until bioanalysis using LC–MS/MS.

For the efficacy study in the SIRS model, six-week-old C57BL/6J male mice received **62** at 1, 2, or 5 mpk (*po*) 30 min before injection with mouse TNF α (iv, 10 μg), then monitored for survival and rectal temperature every hour. The vehicle- or **1**-treated groups were used as controls. For the pharmacodynamic study, mice were anesthetized, perfused, and dissected 8 h after the injection of TNF α (20 μg) on a cryostat, then the organs were collected and sectioned. For immunostaining, tissue sections were mounted and blocked with 10% normal goat serum and 1% BSA, and then incubated with primary antibodies at $4\text{ }^{\circ}\text{C}$ overnight.

For the efficacy study in the IBD model, eight-week-old *Ripk1*^{K612R/K612R}-knockin male mice were administered with **62** at a dose of 10 or 20 mpk (*po*, QD) for continuous 40 days. Mice were monitored every other day for their weights and stool scales. *Ripk1*^{WT} background mice, and the vehicle- or **1**-treated groups were used as controls.

For the efficacy study in the RA model, eight-week-old BALB/c male mice received 1.5 mg (iv) of the anti-collagen antibodies cocktail on Day 0, followed by intraperitoneal injection with LPS (10 μg) on day 3. After 24 h, **62** was administered (*po*) at a dose of 15 or 30 mpk, using the vehicle as a negative control. Mice were weighed and scored every day according to a qualitative scoring system to assess the severity of paw inflammation⁴⁶.

The animal protocols were approved by the Institutional Animal Care and Use Committee of IRCBC, SIOC, and all experiments were performed in accordance with IRCBC, SIOC policies on the care, welfare, and treatment of laboratory animals.

4.8. Statistics

All statistical analyses and curves were performed using the GraphPad software package (La Jolla, CA, USA). Statistical significance between conditions was calculated using a *t*-test (two-tailed) when comparing two groups. All the enzymatic activity assays were performed in triplicate and quantified data were presented as mean \pm SD. IC₅₀ values were calculated using non-linear regression and shown as data points representing mean \pm SD.

4.9. Accession codes

Coordinates and structure factors for the co-crystal structure of RIPK1 kinase domain (1-294, C34A, C127A, C233A, C240A) and **20** have been deposited in the Protein Data Bank with the accession number 812N.

Acknowledgments

We thank Prof. Junying Yuan (IRCBC of CAS, Shanghai, China) and Dr. Jidong Zhu (Etern Therapeutics, Shanghai, China) for their generous help on this work, Dr. Sudan He (ISM of CAMS, Suzhou, China) for providing RIPK3-FKBP NIH/3T3 cells, and National Facility for Protein Science in Shanghai (China) for the help in animal studies. This work was supported by grants from

the National Natural Science Foundation of China (Grants Nos. 21837004, 82151212, and 32170755), the Strategic Priority Research Program of the Chinese Academy of Sciences (XDB39050500, China), Shanghai Municipal Science and Technology Major Project (Grant No.2019SHZDZX02, China).

Author contributions

Conceptualization: Li Tan and Ying Li; Methodology: Li Tan, Ying Li, Ying Qin, Lifeng Pan, Zheng Zhang and, Yechun Xu; Investigation and Formal Analysis: Ying Qin, Dekang Li, Chunting Qi, Huaijiang Xiang, Huyan Meng, Jingli Liu, Shaoqing Zhou, Xinyu Gong, Ying Li, Guifang Xu, Rui Zu, Hang Xie, and Gang Xu; Software: Huaijiang Xiang, Xinyu Gong, and Lifeng Pan; Resources: Shi Chen; Writing-Original Draft: Li Tan, Ying Li, Ying Qin, and Dekang Li; Writing-Review & Editing: All the authors; Supervision: Li Tan, Ying Li, Lifeng Pan, Shi Chen, Zheng Zhang, and Yechun Xu; Funding acquisition: Li Tan, Ying Li, and Zheng Zhang.

Conflicts of interest

Li Tan, Ying Li, Ying Qin, Chunting Qi, and Huaijiang Xiang are inventors on patent applications relating to this work, owned by SIOC, CAS.

Appendix A. Supporting information

Supporting data to this article can be found online at <https://doi.org/10.1016/j.apsb.2023.10.021>.

References

- Ofengeim D, Yuan J. Regulation of RIP1 kinase signalling at the crossroads of inflammation and cell death. *Nat Rev Mol Cell Biol* 2013;**14**:727–36.
- Mifflin L, Ofengeim D, Yuan J. Receptor-interacting protein kinase 1 (RIPK1) as a therapeutic target. *Nat Rev Drug Discov* 2020;**19**:553–71.
- Xu G, Li Y, Zhang S, Peng H, Wang Y, Li D, et al. SARS-CoV-2 promotes RIPK1 activation to facilitate viral propagation. *Cell Res* 2021;**31**:1230–43.
- Shi K, Zhang J, Zhou E, Wang J, Wang Y. Small-molecule receptor-interacting protein 1 (RIP1) inhibitors as therapeutic agents for multifaceted diseases: current medicinal chemistry insights and emerging opportunities. *J Med Chem* 2022;**65**:14971–99.
- Wu Y, Dong G, Sheng C. Targeting necroptosis in anticancer therapy: mechanisms and modulators. *Acta Pharm Sin B* 2020;**10**:1601–18.
- Degterev A, Hitomi J, Gernscheid M, Ch'en IL, Korkina O, Teng X, et al. Identification of RIP1 kinase as a specific cellular target of necrostatins. *Nat Chem Biol* 2008;**4**:313–21.
- Degterev A, Huang Z, Boyce M, Li Y, Jagtap P, Mizushima N, et al. Chemical inhibitor of nonapoptotic cell death with therapeutic potential for ischemic brain injury. *Nat Chem Biol* 2005;**1**:112–9.
- Harris PA, Berger SB, Jeong JU, Nagilla R, Bandyopadhyay D, Campobasso N, et al. Discovery of a first-in-class receptor interacting protein 1 (RIP1) kinase specific clinical candidate (GSK2982772) for the treatment of inflammatory diseases. *J Med Chem* 2017;**60**:1247–61.
- Ren Y, Su Y, Sun L, He S, Meng L, Liao D, et al. Discovery of a highly potent, selective, and metabolically stable inhibitor of receptor-

- interacting protein 1 (RIP1) for the treatment of systemic inflammatory response syndrome. *J Med Chem* 2017;**60**:972–86.
10. Wang W, Marinis JM, Beal AM, Savadkar S, Wu Y, Khan M, et al. RIP1 Kinase drives macrophage-mediated adaptive immune tolerance in pancreatic cancer. *Cancer Cell* 2018;**34**:757–74.e7.
 11. Meng H, Wu G, Zhao X, Wang A, Li D, Tong Y, et al. Discovery of a cooperative mode of inhibiting RIPK1 kinase. *Cell Discov* 2021;**7**:41.
 12. Yoshikawa M, Saitoh M, Katoh T, Seki T, Bigi SV, Shimizu Y, et al. Discovery of 7-oxo-2,4,5,7-tetrahydro-6H-pyrazolo[3,4-c]pyridine derivatives as potent, orally available, and brain-penetrating receptor-interacting protein 1 (RIP1) kinase inhibitors: analysis of structure-kinetic relationships. *J Med Chem* 2018;**61**:2384–409.
 13. Patel S, Webster JD, Varfolomeev E, Kwon YC, Cheng JH, Zhang J, et al. RIP1 inhibition blocks inflammatory diseases but not tumor growth or metastases. *Cell Death Differ* 2020;**27**:161–75.
 14. Harris PA. Inhibitors of RIP1 kinase: a patent review (2016-present). *Expert Opin Ther Pat* 2021;**31**:137–51.
 15. Yang X, Lu H, Xie H, Zhang B, Nie T, Fan C, et al. Potent and selective RIPK1 inhibitors targeting dual-pockets for the treatment of systemic inflammatory response syndrome and sepsis. *Angew Chem Int Ed Engl* 2022;**61**:e202114922.
 16. Xie T, Peng W, Liu Y, Yan C, Maki J, Degtrev A, et al. Structural basis of RIP1 inhibition by necrostatins. *Structure* 2013;**21**:493–9.
 17. Najjar M, Suebsuwong C, Ray SS, Thapa RJ, Maki JL, Nogusa S, et al. Structure guided design of potent and selective ponatinib-based hybrid inhibitors for RIPK1. *Cell Rep* 2015;**10**:1850–60.
 18. Liu Y, Gray NS. Rational design of inhibitors that bind to inactive kinase conformations. *Nat Chem Biol* 2006;**2**:358–64.
 19. Harris PA, Bandyopadhyay D, Berger SB, Campobasso N, Capriotti CA, Cox JA, et al. Discovery of small molecule RIP1 kinase inhibitors for the treatment of pathologies associated with necroptosis. *ACS Med Chem Lett* 2013;**4**:1238–43.
 20. Martens S, Hofmans S, Declercq W, Augustyns K, Vandenabeele P. Inhibitors targeting RIPK1/RIPK3: old and new drugs. *Trends Pharmacol Sci* 2020;**41**:209–24.
 21. Yu X, Ma H, Li B, Ji Y, Du Y, Liu S, et al. A novel RIPK1 inhibitor reduces GVHD in mice via a nonimmunosuppressive mechanism that restores intestinal homeostasis. *Blood* 2023;**141**:1070–86.
 22. Li Y, Zhang L, Wang Y, Zou J, Yang R, Luo X, et al. Generative deep learning enables the discovery of a potent and selective RIPK1 inhibitor. *Nat Commun* 2022;**13**:6891.
 23. Zhu J, Xin M, Xu C, He Y, Zhang W, Wang Z, et al. Ligand-based substituent-anchoring design of selective receptor-interacting protein kinase 1 necroptosis inhibitors for ulcerative colitis therapy. *Acta Pharm Sin B* 2021;**11**:3193–205.
 24. Cuny GD, Degtrev A. RIPK protein kinase family: atypical lives of typical kinases. *Semin Cell Dev Biol* 2021;**109**:96–105.
 25. Mandal P, Berger SB, Pillay S, Moriwaki K, Huang C, Guo H, et al. RIP3 induces apoptosis independent of pronecrotic kinase activity. *Mol Cell* 2014;**56**:481–95.
 26. Wu XN, Yang ZH, Wang XK, Zhang Y, Wan H, Song Y, et al. Distinct roles of RIP1-RIP3 hetero- and RIP3-RIP3 homo-interaction in mediating necroptosis. *Cell Death Differ* 2014;**21**:1709–20.
 27. Canning P, Ruan Q, Schwerdt T, Hrdinka M, Maki JL, Saleh D, et al. Inflammatory signaling by NOD-RIPK2 is inhibited by clinically relevant type II kinase inhibitors. *Chem Biol* 2015;**22**:1174–84.
 28. Hart AC, Abell L, Guo J, Mertzman ME, Padmanabha R, Macor JE, et al. Identification of RIPK3 type II inhibitors using high-throughput mechanistic studies in hit triage. *ACS Med Chem Lett* 2020;**11**:266–71.
 29. Goldstein DM, Gray NS, Zarrinkar PP. High-throughput kinase profiling as a platform for drug discovery. *Nat Rev Drug Discov* 2008;**7**:391–7.
 30. Miduturu CV, Deng X, Kwiatkowski N, Yang W, Brault L, Filippakopoulos P, et al. High-throughput kinase profiling: a more efficient approach toward the discovery of new kinase inhibitors. *Chem Biol* 2011;**18**:868–79.
 31. Hitomi J, Christofferson DE, Ng A, Yao J, Degtrev A, Xavier RJ, et al. Identification of a molecular signaling network that regulates a cellular necrotic cell death pathway. *Cell* 2008;**135**:1311–23.
 32. Terai H, Tan L, Beauchamp EM, Hatcher JM, Liu Q, Meyerson M, et al. Characterization of DDR2 inhibitors for the treatment of DDR2 mutated nonsmall cell lung cancer. *ACS Chem Biol* 2015;**10**:2687–96.
 33. Li X, Zhang M, Huang X, Liang W, Li G, Lu X, et al. Ubiquitination of RIPK1 regulates its activation mediated by TNFR1 and TLRs signaling in distinct manners. *Nat Commun* 2020;**11**:6364.
 34. Yan Xia SC, Czarniecki Michael, Tsai Hsigan, Henry Vaccaro, Cleven Renee, Cook John, et al. Synthesis and evaluation of polycyclic pyrazolo[3,4-d]pyrimidines as PDE1 and PDE5 cGMP phosphodiesterase inhibitors. *J Med Chem* 1997;**40**:4372–7.
 35. Kabsch W. Xds. *Acta Crystallogr D Biol Crystallogr* 2010;**66**:125–32.
 36. Vonrhein C, Flensburg C, Keller P, Sharff A, Smart O, Paciorek W, et al. Data processing and analysis with the autoPROC toolbox. *Acta Crystallogr D Biol Crystallogr* 2011;**67**:293–302.
 37. Tickle IJ, Flensburg C, Keller P, Paciorek W, Sharff A, Vonrhein C, et al. *STARANISO*. Cambridge, United Kingdom: Global Phasing Ltd; 2018.
 38. McCoy AJ, Grosse-Kunstleve RW, Adams PD, Winn MD, Storoni LC, Read RJ. Phaser crystallographic software. *J Appl Crystallogr* 2007;**40**:658–74.
 39. Emsley P, Lohkamp B, Scott WG, Cowtan K. Features and development of Coot. *Acta Crystallogr D Biol Crystallogr* 2010;**66**:486–501.
 40. Liebschner D, Afonine PV, Baker ML, Bunkoczi G, Chen VB, Croll TI, et al. Macromolecular structure determination using X-rays, neutrons and electrons: recent developments in Phenix. *Acta Crystallogr D Struct Biol* 2019;**75**:861–77.
 41. Williams CJ, Headd JJ, Moriarty NW, Prisant MG, Videau LL, Deis LN, et al. MolProbity: more and better reference data for improved all-atom structure validation. *Protein Sci* 2018;**27**:293–315.
 42. Friesner RA, Murphy RB, Repasky MP, Frye LL, Greenwood JR, Halgren TA, et al. Extra precision glide: docking and scoring incorporating a model of hydrophobic enclosure for protein–ligand complexes. *J Med Chem* 2006;**49**:6177–96.
 43. Li X, He Y, Ruiz CH, Koenig M, Cameron MD, Vojtkovsky T. Characterization of dasatinib and its structural analogs as CYP3A4 mechanism-based inactivators and the proposed bioactivation pathways. *Drug Metab Dispos* 2009;**37**:1242–50.
 44. Wang JJ, Guo JJ, Zhan J, Bu HZ, Lin JH. An *in-vitro* cocktail assay for assessing compound-mediated inhibition of six major cytochrome P450 enzymes. *J Pharm Anal* 2014;**4**:270–8.
 45. Kamiya K, Niwa R, Morishima M, Honjo H, Sanguinetti MC. Molecular determinants of hERG channel block by terfenadine and cisapride. *J Pharmacol Sci* 2008;**108**:301–7.
 46. Caplazi P, Baca M, Barck K, Carano RA, DeVoss J, Lee WP, et al. Mouse models of rheumatoid arthritis. *Vet Pathol* 2015;**52**:819–26.